Formation of liquid drops at an orifice and dynamics of pinch-off in liquid jets

Manash Pratim Borthakur,[1] Gautam Biswas,[1,*] and Dipankar Bandyopadhyay[2]
[1]*Department of Mechanical Engineering, Indian Institute of Technology Guwahati, Guwahati 781039, India*
[2]*Department of Chemical Engineering, Indian Institute of Technology Guwahati, Guwahati 781039, India*
(Received 26 March 2017; published 25 July 2017)

This paper presents a numerical investigation of the dynamics of pinch-off in liquid drops and jets during injection of a liquid through an orifice into another fluid. The current study is carried out by solving axisymmetric Navier-Stokes equations and the interface is captured using a coupled level-set and volume-of-fluid approach. The delicate interplay of inertia and viscous effects plays a crucial role in deciding the dynamics of the formation as well as breakup of liquid drops and jets. In the dripping regime, the growth and breakup rate of a drop are studied and quantified by corroborating with theoretical predictions. During the growth stage of the drops, a self-similar behavior of the drop profile is identified over a relatively short duration of time. The viscosity of the drop liquid shows substantial influence on the thinning behavior of a liquid neck and a transition is observed from an inertia dominated regime to an inertia-viscous regime beyond a critical minimum value of the neck radius. The phenomenon of interface overturning is fundamentally related to the magnitude of drop viscosity. The variation of overturning angle as a function of drop viscosity is computed and a critical value of Ohnesorge number is obtained beyond which overturning ceases. Increasing the inertia of drop liquid transforms the system from a periodically dripping regime to a quasiperiodic regime and finally it culminates into an elongated liquid jet. Another interesting transition from dripping to jetting regime is demonstrated by varying the viscosity of the ambient medium. The breakup of jets in Rayleigh mode is explored and the breakup length obtained from our computations shows excellent agreement with the theoretical predictions owing to Rayleigh's analysis. The ambient medium is entrained as the jet moves downstream with the creation of a vortical structure just outside the jet signifying increased participation of the ambient medium in the dynamics of jet breakup at higher inflow rates.

DOI: 10.1103/PhysRevE.96.013115

I. INTRODUCTION

The dynamics of formation and breakup of liquid drops and jets have been studied extensively owing to its rich underlying physics and importance in many industrial applications. A variety of applications involve formation of drops from a nozzle or an orifice, as observed in inkjet printing [1], spray coating [2], separation and extraction processes [3], and others [4]. The success of such technologies rely strongly on the precise and reliable prediction of dynamics related to liquid column breakup as well as subsequent drop formation.

The formation of drops from vertical capillary tubes has been studied experimentally [5–11] and computationally [9–19] by many researchers. The process of drop formation is widely classified into two categories: dripping and jetting. In the dripping regime, which occurs at low flow rates, the drops periodically form near the orifice. As the flow rate is slowly increased, the nonlinear effects come into the picture resulting in a quasiperiodic pattern of drop formation characterized by regularly repeating multiple detached drop volumes and limiting drop lengths. At sufficiently high flow rates, the system transitions into jetting mode where the inertia force becomes a dominating factor and drops break up from the end of a long jet of liquid, which is inherently unstable. The dynamics of growth and breakup in the dripping mode has been explored experimentally by several researchers [5–11,16,20,21]. Besides experimental investigations, numerical studies on drop formation in air has been conducted using one-dimensional (1D) slender jet approximations [9,11–13], boundary integral methods [14,15], and solution of full Navier-Stokes equations [17–19,22]. The pioneering work by Savart [23], Plateau [70], and theoretical analysis of Rayleigh [24,25] provided a basic understanding of the instability of jets and predictions of important parameters, such as the breakup length and drop diameter. Subsequently, many investigations have been performed theoretically [26–33], experimentally [34–41], and numerically [19,42–46] to uncover the fascinating aspects of the jetting mode and its associated dynamics.

The present paper is an attempt to analyze a few salient features of drop formation in both dripping and jetting regimes by solving the full Navier-Stokes equations under axisymmetric conditions. For this purpose, we have used an in-house interface-capturing code based on the coupled level-set and volume-of-fluid (CLSVOF) method. The code has been previously successfully applied to simulate two-phase flows [47–53]. We demonstrate the influence of inertia and viscous effects on the pinch-off of liquid drops. An interesting transition from dripping to jetting is presented by varying the viscosity of the ambient medium. Finally, breakup of jets in the Rayleigh mode is explored and entrainment of ambient medium is demonstrated for jets moving at high velocity.

The rest of the paper is organized as follows. In Sec. II, we outline the formulation of the problem and discuss the validation of the present numerical solver in Sec. III. The results are presented in Sec. IV and concluding remarks are given in Sec. V.

II. FORMULATION OF THE PROBLEM

A. Computational domain

A representative diagram of the computational domain adopted is shown in Fig. 1. The drop liquid of density ρ_i

*gtm@iitg.ernet.in

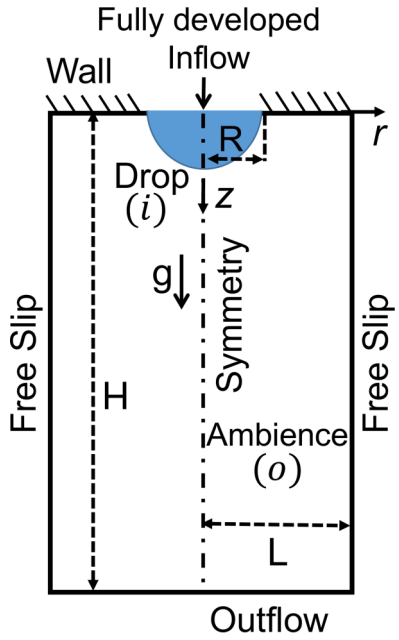

FIG. 1. Schematic diagram (not to scale) showing the computational domain and boundary conditions in cylindrical coordinate system (r,z,θ). A fully developed flow is imposed at the orifice inlet of radius R initialized with a hemispherical drop. Gravity acts along positive z axis. The size of the domain is taken as $5R$ in radial (r) direction whereas 30–$60R$ in axial (z) direction

and viscosity μ_i is injected through an orifice of radius R on a horizontal wall at a constant flow rate, $\dot{Q}_d$ into a quiescent ambience at density ρ_o and viscosity μ_o. The surface tension σ is assumed to be spatially uniform and constant with time. A cylindrical coordinate system (r,z,θ) is adopted considering the dynamics to be axisymmetric so that the problem is independent of θ where (r,z,θ) are the radial coordinate, axial coordinate, and azimuthal angle, respectively. The origin is chosen at the center of the orifice and gravity aligns in the direction of the z axis. The size of the computational domain is taken as $5R$ in the radial direction and 30–$60R$ in the axial direction so as to ensure that the results are not influenced by the outflow boundary conditions. The three-phase contact circle where the drop base, outer ambience, and orifice rim meet, remains pinned to the sharp edge of the orifice and hence no contact angle needs to be specified in this problem.

B. Governing equations and numerical procedure

In this study a Newtonian liquid drop is injected into another Newtonian liquid and both fluids are considered immiscible and incompressible. The problem is governed by the single set of continuity and Navier-Stokes equations for treating a single fluid continuum. The continuity equation is given as

$$\nabla \cdot \mathbf{v} = 0, \tag{1}$$

where, $\mathbf{v} = (u,v)$ are axial and vertical components of the velocity field, respectively. The momentum equation is

$$\rho(\tilde{\alpha})(\partial \mathbf{v}/\partial t + \nabla \cdot \mathbf{vv}) = -\nabla P + \rho(\tilde{\alpha})\mathbf{g} + \nabla \cdot [\mu(\tilde{\alpha})(\nabla \mathbf{v} + \nabla \mathbf{v}^{\mathbf{T}})] + \sigma\kappa(\phi)\nabla\tilde{\alpha}. \tag{2}$$

The influence of surface tension is incorporated into the momentum equations following the continuum surface force (CSF) model of Brackbill *et al.* [54]. Here, $\tilde{\alpha}$ is the smoothed void fraction field, which is defined using a Heaviside function [55] $H(\phi)$ as

$$\tilde{\alpha} = H(\phi) = \begin{cases} 0 & \text{if } \phi < -\epsilon \\ \frac{1}{2} + \frac{\phi}{2\epsilon} + \frac{1}{2\pi}\left[\sin\left(\frac{\pi\phi}{\epsilon}\right)\right] & \text{if } |\phi| \leqslant \epsilon \\ 1 & \text{if } \phi > \epsilon \end{cases}. \tag{3}$$

The symbol ϕ defines the level-set function, which is the signed distance function from the interface. The value of ϕ is zero at the interface, it assumes positive value in the liquid 1 region and negative value in the liquid 2 region. Here, 2ϵ is the interface thickness over which the fluid properties are interpolated. The present simulations were performed using $\epsilon = 1.5\,\delta x$, where δx is the size of the computational cell. The smoothed density $\rho(\tilde{\alpha})$ and viscosity $\mu(\tilde{\alpha})$ can be expressed by a Heaviside function $H(\phi)$

$$\rho(\tilde{\alpha}) = \rho_i\tilde{\alpha} + \rho_o(1-\tilde{\alpha}) \tag{4}$$

$$\mu(\tilde{\alpha}) = \mu_i\tilde{\alpha} + \mu_o(1-\tilde{\alpha}), \tag{5}$$

where, i and o represent inner drop liquid and outer ambient fluid, respectively. The density and viscosity of both fluids are assumed to be constant. The local curvature κ at the air-liquid interface is computed as

$$\kappa = -\nabla \cdot \hat{\mathbf{n}}, \tag{6}$$

where the unit normal vector $\hat{\mathbf{n}}$ derived from level-set function ϕ

$$\hat{\mathbf{n}} = \frac{\nabla\phi}{|\nabla\phi|} \tag{7}$$

and it is directed into the external fluid. In the CLSVOF method, the advection equation for the volume fraction α and the level-set function ϕ are

$$\frac{\partial\alpha}{\partial t} + \nabla \cdot (\mathbf{v}\alpha) = 0, \tag{8}$$

$$\frac{\partial\phi}{\partial t} + \nabla \cdot (\mathbf{v}\phi) = 0. \tag{9}$$

The interface is considered as a piecewise linear segment in each cell. The level-set function ϕ [56] is used to capture the interface and volume fraction of the liquid α [57] is deployed to conserve mass due to the moving interface. The governing equations are discretized using the finite-difference method on a cylindrical coordinate and equidistant grid $\delta r = \delta z$ in the radial and axial directions. The MAC algorithm [58] is employed to solve the single set of governing equations on a staggered grid with scalars (ρ,α,ϕ) located at the cell centers and velocity components at the center of the cell faces. The convection and the viscous terms are discretized by a second-order ENO method [59] and central differencing, respectively. In the present paper, the time-stepping procedure is based on the explicit method and hence to maintain the stability of the solution, time steps are chosen to satisfy CFL, capillary, viscous, and gravitational time conditions [47]. The detailed numerical methods have been described by Gerlach *et al.* [60]. The CLSVOF method has been used by many researchers

successfully for solving variety of problems involving the study of dynamics of buoyancy-driven gas bubbles' motion in a quiescent liquid and the dynamics of bubble formation from a submerged orifice [47–49], impact of a drop on a liquid surface [51], bubble entrapment owing to drop impact [50], and many such problems of scientific interest [61,62].

C. Boundary conditions

At the orifice inlet, a parabolic velocity profile is imposed satisfying the conditions of desired liquid injection rate.

$$u(r) = 0, \quad v(r) = 2v_{\text{avg}}\,[1 - (r/R)^2], \quad \alpha = 1 \quad \text{for } 0 \leqslant r \leqslant R, \tag{10}$$

where u and v are the radial and axial velocity components, respectively. For the outflow boundary, it is assumed that influence of upstream is minimum, i.e., there is no change in axial direction.

$$\frac{\partial u}{\partial z} = \frac{\partial v}{\partial z} = \frac{\partial \alpha}{\partial z} = \frac{\partial \phi}{\partial z} = 0, \quad P = P_0. \tag{11}$$

Due to the axisymmetric nature of the problem, the normal components of velocity and the viscous shear stress vanish along the axis of symmetry.

$$u = 0, \quad \frac{\partial v}{\partial r} = \frac{\partial \alpha}{\partial r} = \frac{\partial \phi}{\partial r} = 0. \tag{12}$$

At the solid wall, liquid obeys conditions of no slip and no penetration,

$$u = v = 0 \quad \text{for } R \leqslant r \leqslant L. \tag{13}$$

D. Initial conditions

The drop is initially assumed to be a hemisphere of radius equal to that of the orifice radius. The initial state of the static drop can be defined as

$$r^2 + z^2 = R^2. \tag{14}$$

Both the drop and ambience are considered to be initially quiescent and at uniform pressure.

$$u = v = 0, \quad P = \text{const at } t = 0 \tag{15}$$

E. Nondimensional parameters

The nondimensional parameters pertinent to our problem are the Weber number, Bond number, and Ohnesorge number given as:

$$\text{We} = \frac{\rho_i {v_{\text{avg}}}^2 R}{\sigma} \tag{16}$$

$$\text{Bo} = \frac{\rho_i g R^2}{\sigma} \tag{17}$$

$$\text{Oh} = \frac{\mu_i}{\sqrt{\rho_i R \sigma}}. \tag{18}$$

The Weber number, We, measures the importance of inertia force relative to the surface tension force; the Bond number,Bo, measures the importance of gravity force relative to surface tension force; and the Ohnesorge number, Oh, measures the relative importance of viscous force over inertia and surface tension forces.

Two other nondimensional parameters, the density ratio η and viscosity ratio λ, are introduced to account for the dynamic effect of surrounding medium on the drop formation.

$$\eta = \frac{\rho_o}{\rho_i}, \tag{19}$$

$$\lambda = \frac{\mu_o}{\mu_i}. \tag{20}$$

The following dimensionless characteristic variables are introduced:

$$z^* = \frac{z}{R}, \quad r^* = \frac{r}{R}, \quad v^* = \frac{v}{v_{\text{avg}}}, \quad P^* = \frac{P}{\rho_i {v^2}_{\text{avg}}}, \quad t^* = t\frac{v_{\text{avg}}}{R}, \tag{21}$$

where the orifice radius R is the characteristic length scale and average velocity of liquid at inlet, $v_{\text{avg}} = \dot{Q}_d/\pi R^2$ is the characteristic velocity scale.

F. Fluid properties

The drop fluid is chosen to be an aqueous solution of glycerine in varying concentrations. The surrounding medium is considered as air for most of the simulations. However, in Sec. IV D, the surrounding medium is considered as organic oil to demonstrate the effect of viscosity of the ambient medium on the dynamics.

III. VALIDATION OF CURRENT NUMERICAL APPROACH

A. Comparison with experiments

Figure 2 presents a comparison of the drop shape at the incipience of breakup predicted by our current computations

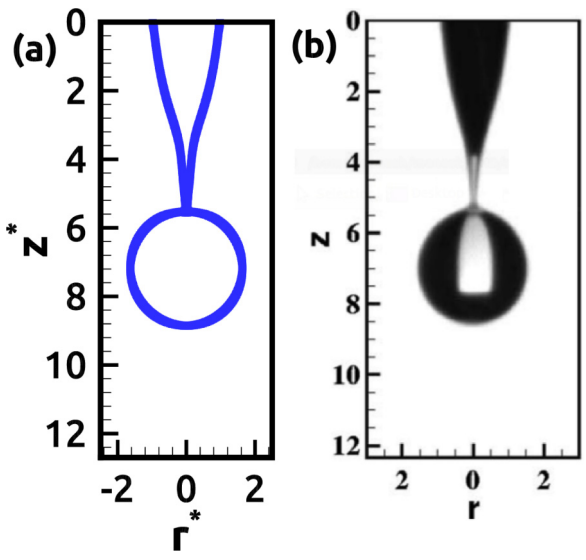

FIG. 2. Qualitative comparison of drop formation between (a) current computations and (b) experimental results of Subramani *et al.* [9] under conditions of Oh = 0.13, Bo = 0.33, We = 0.119, η = 0.001, and λ = 0.0005.

TABLE I. Quantitative comparison of drop formation between current computations and experimental results of Subramani *et al.* [9] under conditions of Oh = 0.13, Bo = 0.33, We = 0.119, $\eta = 0.001$, and $\lambda = 0.0005$.

Parameters	Experimental	Present Computation
Limiting length L_d^*	8.6 ± 0.1	8.45
Drop Volume V_d^*	17.4 ± 0.3	17.44

with the experimental results of Subramani *et al.* [9]. The comparison shows excellent qualitative agreement of our computational results with experimental observations.

The values of dimensionless limiting length ($L_d{}^* = L_d/R$) and dimensionless detached volume ($V_d{}^* = V_d/R^3$) depicted in Fig. 2 are calculated and presented in Table I in order to make a quantitative comparison with Subramani *et al.* [9]. The experimentally obtained values of $L_d{}^*$ and $V_d{}^*$ are $L_{d,\mathrm{exp}}{}^* = 8.6 \pm 0.1$ and $V_{d,\mathrm{exp}}{}^* = 17.4 \pm 0.3$. The corresponding values obtained from our computations are $L_{d,\mathrm{comp}}{}^* = 8.45$ and $V_{d,\mathrm{comp}}{}^* = 17.44$, which are in excellent agreement with the experiments.

B. Grid convergence studies

To ensure that the results obtained from our computations are independent of grid resolution, we chose five grid sizes ($25 \times 150, 50 \times 300, 80 \times 480, 100 \times 600, 125 \times 750$). The test was conducted under conditions of Oh = 0.003, Bo = 0.18, We = 0.8, $\eta = 0.001$, and $\lambda = 0.02$. The dimensionless drop volume V_d^* is compared for the five chosen grids as tabulated in Table II. It was observed that the difference of V_d^* between grids 25×150 and 50×300 is around 2% whereas the difference between grids 100×600 and 125×750 is less than 0.1%. Arising out of computational experiments, we have chosen grid size of 100×600 for our present computations to optimize computational time without compromising the accuracy of the results.

IV. RESULTS AND DISCUSSION

This section presents the results from our simulations to uncover the dynamics of formation and breakup of liquid drops and jets injected in a quiescent medium from an orifice. The range of values for the governing dimensionless numbers explored in the simulations are listed in Table III.

TABLE II. Comparison of dimensionless drop volume V_d^* for different grid sizes [$25 \times 150, 50 \times 300, 80 \times 480, 100 \times 600, 125 \times 750$]. The relevant conditions are Oh = 0.003, Bo = 0.18, We = 0.8, $\eta = 0.001$, and $\lambda = 0.02$.

Grid Points	Drop volume (V_d^*)	Percent change (%)
25×150	29.74	–
50×300	30.44	2.35
80×480	30.98	1.77
100×600	31.20	0.71
125×750	31.24	0.12

TABLE III. Range of dimensionless numbers employed for the numerical simulations.

Dimensionless parameter	Range
We	0.1–9.5
Bo	0.18
Oh	0.002–0.2
η	0.001 and 0.74
λ	0.0001–15.0

A. Drop growth

The temporal evolution of the drop is termed as drop growth history. Due to continuous injection of the liquid through the orifice, the size of the drop increases with time and finally detaches under the action of gravity. Figure 3 shows the drop growth history as a function of time. Here, D_d^* and t^* represent the nondimensional drop diameter and time, respectively, where $D_d^* = D_d/R$. For a constant flow rate of the liquid through the nozzle, $V_d = V_s + \dot{Q}_d t$, where V_d and V_s are the instantaneous and initial drop volumes and $\dot{Q}_d$ is the constant rate of liquid injection. Assuming the drop remains spherical throughout the growth process, the drop volume is given by $V_d = (\pi/6)D_d^3$ and hence the dimensionless drop diameter is calculated from the growth law using Eq. (22). The growth law from our numerical simulation is found to be $D_d^* = (4.009 + 5.940t^*)^{1/3}$, which is in excellent agreement with the theoretical prediction of Eq. (22).

$$D_d^* = (4 + 6t^*)^{1/3}. \tag{22}$$

Considering the initial stage of the drop growth, a self-similarity analysis of the profile of the growing drop is performed. The fitting function used is of the form $z^*/t^{*\alpha} = ar^*t^{*\beta}$ where z^* and r^* are the nondimensional quantities defined earlier and α and β are the exponents [62]. The relationship between α and β is followed as $\alpha = 1 - \frac{2}{5}\beta$. The constant a is considered as unity and the values of α and β are 0.40 and 0.15, respectively. The results obtained from simulation of drops of different viscosities are presented

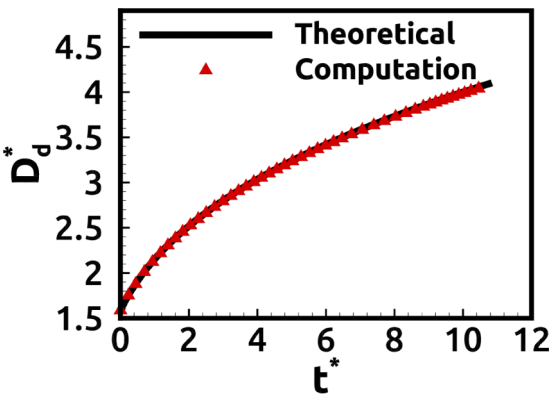

FIG. 3. Numerical prediction of dimensionless drop diameter D_d^* as a function of dimensionless time t^* and comparison with analytical expression Eq. (22) for Oh = 0.003, Bo = 0.18, We = 0.2, $\eta = 0.001$, and $\lambda = 0.02$.

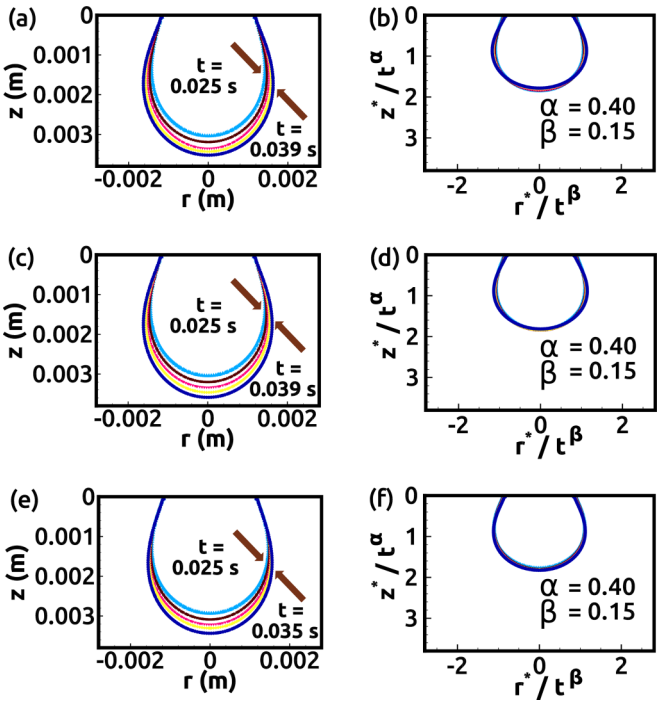

FIG. 4. (a) Instantaneous interface profiles and (b) collapsed profiles during drop growth stage from $t = 0.025$s to $t = 0.039$s for Oh $= 0.002$,Bo $= 0.18$,We $= 0.2$,$\eta = 0.001$,$\lambda = 0.02$. (c) Instantaneous interface profiles and (d) collapsed profiles during drop growth stage from $t = 0.025$s to $t = 0.039$s for Oh $= 0.014$,Bo $= 0.18$,We $= 0.2$,$\eta = 0.001$,$\lambda = 0.004$. (e) Instantaneous interface profiles and (f) collapsed profiles during drop growth stage from $t = 0.025$s to $t = 0.035$s for Oh $= 0.1$,Bo $= 0.18$,We $= 0.2$,$\eta = 0.001$,$\lambda = 0.0006$. The axes has been rescaled following $z^*/t^{*\alpha} = ar^*t^{*\beta}$.

in Fig. 4. For values of Oh $= 0.002$ and 0.014 shown in Figs. 4(a)–4(b) and 4(c)–4(d), respectively, the growing drop profile collapses on a single curve between time instants $t = 0.025$s and $t = 0.039$s. The higher magnitude of α over β indicates that the growth of the drop in the axial direction is faster than the radial direction due to the constant inflow imposed at the orifice. However, at a higher value of Oh $= 0.1$ shown in Figs. 4(e)–4(f), the growth follows self-similarity but for a smaller time range between $t = 0.025$s and $t = 0.035$s. The numerical experiments demonstrates that the growth of the drop accelerates due to the dominance of the viscous forces over the surface tension forces at higher Oh.

B. Drop breakup

A salient feature of drop formation is the occurrence of a slender neck that connects the about-to-form drop with the rest of the fluid attached to the orifice. It is interesting to analyze the relation between the minimum radius of the neck ($r^*_{\min} = r^*_{\text{neck}}$) and time leading to drop pinch-off where $r^*_{\min} = r_{\min}/R$. The temporal decrease of the neck radius $r^*_{\min}$ with time t^* can be characterized by the power-law expression $r^*_{\min} \sim \tau^\alpha$ where τ is the time leading to drop pinch-off [$\tau = (t_{\text{pinch}} - t)/t_c$]. Here, $t_c = \sqrt{\rho R^3/\sigma}$ is the capillary time scale and α is the effective exponent of the power law. In

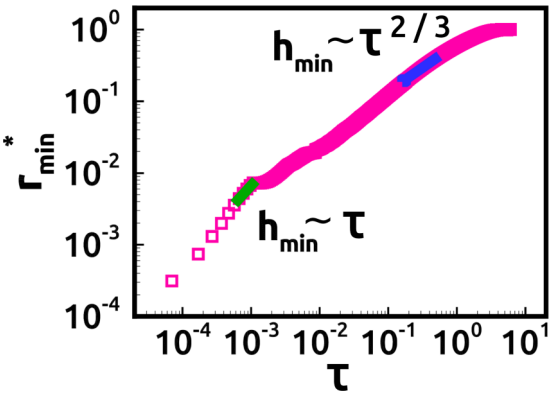

FIG. 5. Relation between minimum neck radius $r^*_{\min}$ and time before pinch-off τ during collapse stage. The solid line represents $r^*_{\min} \sim \tau^{2/3}$. Parameters are Oh $= 0.003$, Bo $= 0.18$, We $= 0.2$, $\eta = 0.001$, and $\lambda = 0.02$.

the present investigation, the drop is assumed to pinch off when $r^*_{\min}$ falls below 0.001, i.e., the size of a single grid cell. Previously, Basaran [4] suggested that a thinning filament undergoes transition from either an initial inertia or viscosity dominated regime to an inertia-viscous regime close to the instant of pinch-off. In the present investigation, Oh $= 0.003$, which signifies that viscous forces are weak and hence initial thinning of the neck takes place under an inertia dominated regime. The results from Fig. 5 clearly indicate the value of α to be $2/3$ in the inertia dominated regime, which agrees well with the predictions of Basaran [4]. However, as the neck radius $r^*_{\min}$ falls below 0.008, the viscous effects come into play and the thinning process is brought about in an inertia-viscous regime with $r^*_{\min} \sim \tau$. The results closely match the transitional phenomenon reported earlier by Chen *et al.* [17] and Rothert *et al.* [63].

The shape of the interface at the instant of pinch-off is critically dependent on the viscosity of drop liquid. For drops of low viscosity, the interface folds on itself with an internal angle greater than 90○ thereby making the interface a multivalued shape function and this phenomenon is called overturning. However, the interface overturning is arrested when the viscosity of the droplet increases beyond a critical value.

The overturning of the drop interface can be explained by studying the velocity field inside the drop just prior to breakup as shown in Fig. 6 . As the neck collapses, the fluid is expelled rapidly into the drop hanging below and the velocity increases along the centerline. For a low viscous drop such as pure water, the dissipation of the shear stress arising out of rapid fluid movement near the centerline is substantially weak. This results in a velocity gradient across the drop with the fluid velocity decreasing progressively towards the outer periphery. The drop interface thus folds onto itself as it approaches the moment of pinch-off. However, for a highly viscous drop, the velocity profile resembles that of a plug flow with an almost negligible velocity gradient across the drop. Accordingly, the interface maintains its smooth curvature and does not overturn. These results from our computations corroborate the findings of Wilkes *et al.* [64].

A parametric study of the overturning phenomenon is carried out by varying Oh in order to reveal the critical value

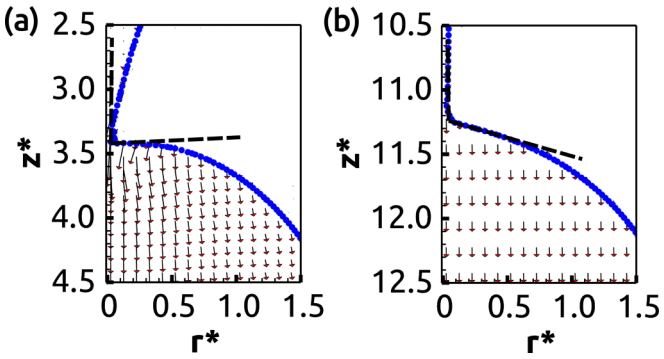

FIG. 6. Velocity field inside drop of (a) pure water (b) 91% glycerine. Only selected velocity vectors are plotted to maintain clarity. It is seen that interface overturning occurs for a pure water drop whereas it vanishes for highly viscous drops.

of Oh at which overturning vanishes. Day *et al.* [65] and Casterjón-Pita *et al.* [66] showed that the drop interface at breakup for low Oh adopts a unique double cone shape with large and small angles of 112.8○ and 18.1○, respectively. They proposed that the breakup remains self-similar with the interface approaching these unique angles irrespective of initial flow conditions or type of breakup. However, these studies were carried out for either inviscid or low-viscosity drops. In the present investigation, the variation of large (θ_l) and small (θ_s) angles due to increasing viscosity of the drop liquid is captured and presented in Fig. 7 . It can be clearly observed that both the angles predicted by the present computations agree well with the values of Day *et al.* [65] and Casterjón-Pita *et al.* [66] for lower values of Oh. However, the angles deviate significantly from the predicted [65,66] values of 112.8○ and 18.1○ and show a decreasing trend with increasing Oh. The value of θ_l ranges between 111.3○ and 85.3○ whereas θ_s varies between 13.5○ and 7.6○ when Oh is altered from 0.002 to 0.1. The overturning phenomenon vanishes when θ_l falls below 90○ and this occurs at a critical value of Oh = 0.075. It is to be noted that the values of θ_l and θ_s at the near-inviscid limit of Oh = 0.002 show slight deviation from the predictions of Day *et al.* [65]. This deviation may be attributed to the small yet finite effects of viscosity at Oh = 0.002.

C. Inertia driven dripping-to-jetting transition

The effect of inflow rate on the drop formation process is studied in detail. The Weber number signifies the increase of inertia force relative to surface tension force. At low We, the drop forms periodically close to the orifice and this regime is called dripping. With increasing We, the higher inertia force pushes the pendant drop further downwards producing a long elongated liquid column and the system finally transits into a jetting regime. Also, the increased inertia force reduces drop formation time and subsequently the drop volume.

Figure 8 illustrates the effect of increasing Weber number on the dynamics of the droplet formation process. At We = 0.2, the drop formation, which occurs in the dripping regime, is characterized by a very short liquid column and almost constant limiting length of breakup (L_d) as shown in

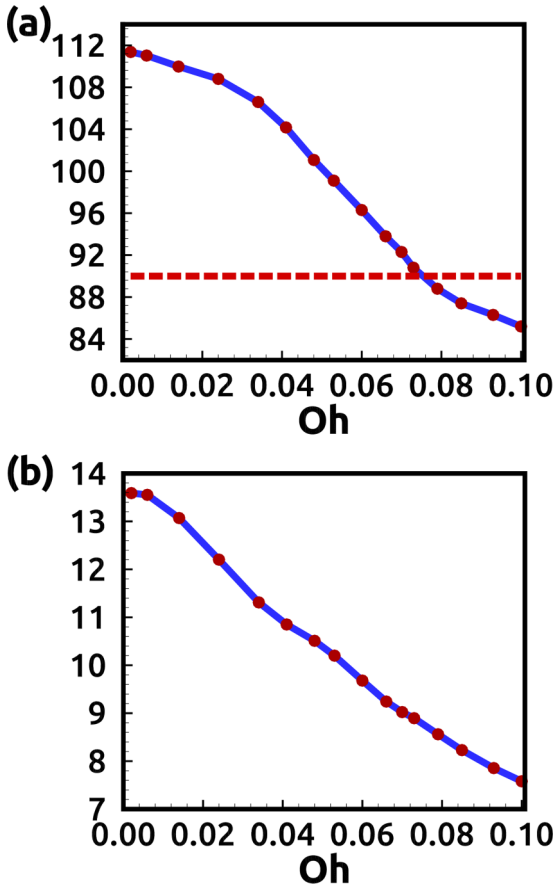

FIG. 7. Effect of Oh on the overturning angles at pinch-off (a) large angle (b) small angle. The dashed line represents the limit when overturning vanishes ($\theta_l = 90^\circ$). The other relevant parameters are Bo = 0.18, We = 0.2, $\eta = 0.001$, and $\lambda = 0.02$–0.0006.

Figs. 8(a)–8(d). The drop volume and time period between two successive drop breakup is almost constant suggesting a periodic formation process. As We is increased to 1.0, the time period between successive drop breakups becomes slightly irregular and gets significantly reduced. Although the limiting length of breakup (L_d) is almost constant, the drops formed are of unequal volume and the process can be characterized as a quasiperiodic dripping process. It can be noted from Figs. 8(e)–8(h) that due to reduced drop formation time, multiple drops can be observed within an axial distance of $z^* = 30$ considered as the length of our computational domain. However, the slow formation process at We = 0.2 ensures that the previously released drop crosses the entire computational domain before another drop gets detached as observed in Figs. 8(a)–8(d). On the other hand, the drop formation at We = 2.0 clearly falls under a jetting regime where a long column of liquid finally breaks into drops often in an aperiodic manner. Figures 8(i)–8(l) demonstrates the breakup of a liquid column and subsequent drop formation in the jetting regime. It can be clearly perceived that the jet length at breakup fluctuates with time and drop formation occurs with unequal time intervals. Axisymmetric wavelike perturbations are seen developing on the surface of the liquid jet as it moves downstream. This results in a big drop being

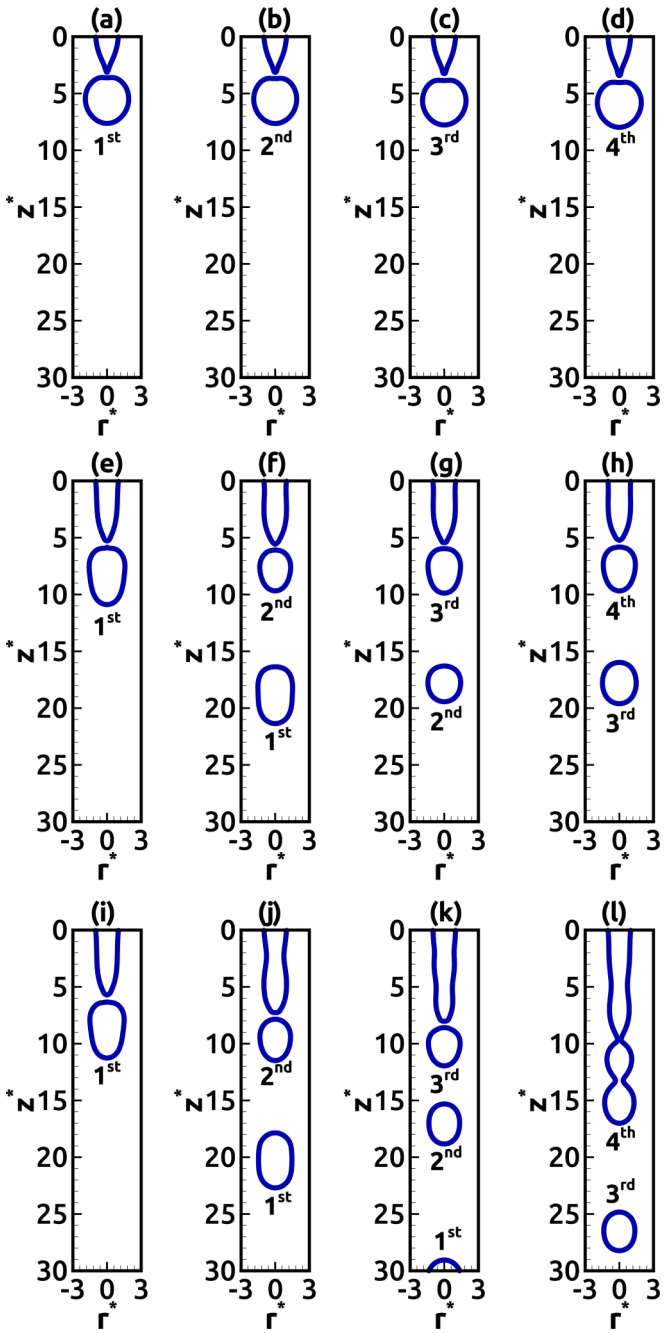

FIG. 8. Effect of Weber number on the droplet formation process. (a)–(d) shows the drop formation for We = 0.2 at time t^* 10.90, 20.83, 30.92, and 41.30, respectively. (e)–(h) shows the drop formation for We = 1.0 at time t^* 11.50, 16.89, 22.22, and 27.50, respectively. (i)–(l) shows the drop formation for We = 1.2 at time t^* 11.05, 17.15, 21.30, and 28.82, respectively. Other parameters remain fixed at Oh = 0.003, Bo = 0.18, $\eta = 0.001$, and $\lambda = 0.02$.

disintegrated as shown in Fig. 8(l). The dynamics of jetting are further discussed in Sec. IV E.

The important parameter of interest is the critical Weber number at which the system transitions from dripping to jetting regime. In order to understand the mechanistic reasons for this transition, we apply some of the scaling laws proposed by Ambravaneswaran *et al.* [11]. It was proposed that the transition can be explained in terms of the relevant characteristic time scales of the dynamics. For low Oh drops, the time scale for capillary breakup scales as $t_c \sim \sqrt{\rho R^3/\sigma}$ whereas the time scale for flow scales as $t_f \sim R/U$. The flow time scale can also be termed as advection time scale. It is expected that the transition occurs when the advection time scale jumps the capillary breakup scale. In our present computations, parameters are fixed as Oh = 0.003 and Bo = 0.18. This gives a capillary time scale of $t_c = 4.656$ ms, which does not vary with Weber number. However, the advection time scale varies with increasing We. For We = 0.2, $t_f = 10.41$ ms, which is greater than t_c whereas for We = 2.0, $t_f = 3.29$ ms, which is smaller than t_c. Thus, the transition of the system from dripping to jetting occurs as the time scale of flow t_f decreases below the capillary time scale for breakup of a given particular system. By equating the advection time scale with capillary time scale for the system of interest in our study, we obtain the critical Weber number for transition as We $\sim$ 1.0, which seems to be in perfect agreement with our computational results reported herein. This criterion can hence be very useful to understand and correctly predict the system response at varying conditions of Weber numbers.

D. Viscosity-driven dripping-to-jetting transition

Another class of dripping-to-jetting transition is driven by the viscous interaction of the jet with outer ambient fluid. When the surrounding exterior is filled with a viscous fluid, such as organic oil, the interface of the liquid column emanating from the orifice experiences a very high drag force from the ambient fluid, which tends to pull it downstream whereas the surface tension force tends to hold the liquid close to the orifice. At lower values of viscosity ratio λ, the surface tension force is strong enough to maintain a dripping mode of drop formation. However, as λ increases beyond a critical value, the viscous drag starts dominating and finally induces transition to a long jet. The entire transition from dripping to jetting driven by viscosity of ambient medium is presented in Fig. 9.

It can be clearly observed from Figs. 9(a) and 9(b) that for $\lambda = 7.5$ and 10.0, the drop formation occurs in dripping mode with a small liquid neck connecting the drop to the orifice. The limiting length at breakup L_d^* shown in Fig. 9(d) increases by $\sim$19% when λ is varied from 7.5–14.0. However, as λ increases from 14.0–15.0, L_d^* abruptly increases by almost $\sim$30% thereby signaling transition to a jetting mode. Udata *et al.* [67] studied dripping to jetting transitions in coflowing conditions using liquid-liquid systems. They demonstrated that transition to jetting mode can be triggered by increasing the flow rate of either the inner or outer fluid. The transition was thus categorized as inertia or viscosity driven similar to our observations. However, the viscosity-driven transition demonstrated in our results shows an entirely different behavior from what is reported in Utada *et al.* [67]. The liquid jet shows a progressively slender diameter as it moves downstream and the size of the resulting drops is comparable to the orifice diameter. In the present investigation, the shape of the liquid jets in the jetting regime does not become narrow as they move downstream. The size of the resulting drops is also much bigger than the orifice diameter. Interestingly, in both the cases as stated above, the dominant viscous effects bring

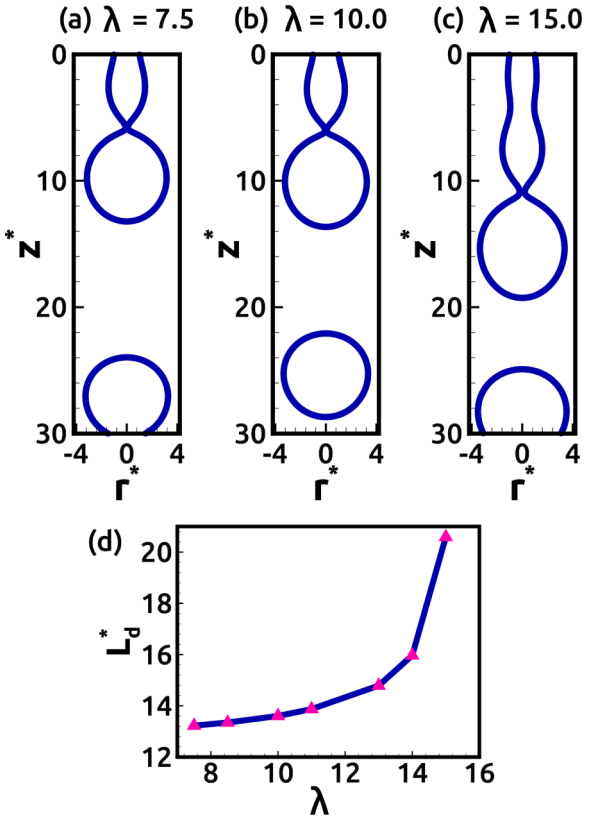

FIG. 9. Transition from dripping to jetting regime with variation of viscosity ratio λ. (a) and (b) shows the drop formation in dripping mode for $\lambda = 7.5$ and 10.0, respectively. (c) shows the jetting regime at $\lambda = 15.0$. (d) shows the variation of limiting length at breakup L_d^* with increasing λ. Other parameters remain fixed at Oh = 0.02, We = 0.4, Bo = 0.18, and $\eta = 0.74$.

about the transition to jetting mode. However, in the case of present investigation, the effect of motion of the ambient fluid is negligible and hence the jet shows a profoundly different behavior from that of Utada *et al.* [67].

In order to understand the dynamical reasons for the transition, the competition between inertia and viscous forces against surface tension force is considered. The inertia force of the inner liquid scales as $F_I \sim \rho_i v_{\text{avg}}^2 R^2$ whereas the viscous drag due to the exterior fluid is given as $F_V \sim \mu_o v_{\text{avg}} R$, where R is the radius of orifice and v_{avg} is the average inflow velocity of drop liquid. The surface tension force scales as $F_S \sim \sigma R$. The transition from dripping to jetting takes place when the combined effect of inertia force F_I and viscous force F_V outweighs the surface tension force F_S, i.e., $F_I + F_V \geqslant F_S$. This can be recast in a nondimensional form as $\text{We} + Ca_o \geqslant O(1)$, where We is the Weber number of inner fluid defined in Sec. II E and $Ca_o = \mu_o v_{\text{avg}}/\sigma$ is the capillary number of the exterior fluid. In the present investigation, the We remains fixed at 0.4. However, Ca_o increases as the viscosity ratio λ is increased by changing μ_o. The value of $\text{We} + Ca_o$ for $\lambda = 7.5$ under the conditions of Oh = 0.02, We = 0.4, Bo = 0.18, and $\eta = 0.74$ comes out to be 0.5, which lies in the dripping regime. However, the value of $\text{We} + Ca_o$ increases to 0.9 when λ is increased to 20.0, which lies in the jetting regime. Thus, the increasing dominance of viscous effect of ambient fluid causes transition from dripping-to-jetting and the results from the present computations agree well with the proposed theoretical criterion for viscosity driven transition.

E. Jet breakup

A liquid jet emanating from a nozzle is inherently unstable and finally breaks up into small droplets to minimize its surface tension. The stability of a jet is influenced by a host of parameters such as the properties of the liquid, inflow rate, and ambient conditions, among others. A series of transitions occurs between different instability regimes, which profoundly affect the evolution and breakup of a jet. Four major breakup regimes of jets have been established [68] and are named as the Rayleigh regime, the first wind-induced regime, the second wind-induced regime, and the atomization regime. The Rayleigh instability regime [24] is initiated by the growth of small amplitude perturbations on the liquid surface leading to varicose deformation of the jet. As the inflow rate is increased, the breakup mode shifts to first wind-induced regime where the ambient medium starts interacting leading to asymmetric disturbances in the form of sinuous deformation. Further increase of inflow condition causes the formation of ligaments and smaller drops, which break up from the liquid jet. The diameters of these fragments are comparable with the jet diameter in the second wind-induced regime. Finally, transition to atomization occurs where fine drops are formed due to further breakup of ligaments and drops. These ligaments have undulated surfaces. The undulations (usually varicose) grow and breakup of the ligaments is brought about by the Rayleigh-Plateau instability mechanism entailing creation of droplets of even smaller sizes.

The present computations are performed for jet breakup in the Rayleigh mode as the axisymmetric assumption remains valid in this regime. The limiting length of the jet at breakup (L_d) serves as a convenient parameter for studying the dynamics in the jetting regime. As the inflow rate is increased, L_d keeps increasing due to higher inertia of the jet. The criterion for predicting different breakup regimes have been reviewed by Chigier and Reitz [69]. It was suggested that breakup under Rayleigh regime occurs when

$$\text{We}_l > 8 \quad \text{and} \quad \text{We}_g < 0.4, \tag{23}$$

where $\text{We}_l = \rho_l {v_{\text{avg}}}^2 2R/\sigma$ and $\text{We}_g = \rho_g {v_{\text{avg}}}^2 2R/\sigma$ are the liquid and gas Weber numbers, respectively.

The pioneering work of Plateau and Rayleigh [24,70] on jet instability can be summarized in the form of a dispersion equation, which captures the dependence of growth rate of disturbance ω on the wave number k as [71]

$$\omega^2 = \frac{\sigma}{\rho_l R^3} kR \frac{I_1(kR)}{I_0(kR)}(1 - k^2R^2). \tag{24}$$

Here, $I_0(kR)$ and $I_1(kR)$ are the modified Bessel functions of the first kind of zeroth and first order, respectively, and R is the radius of the cylindrical jet. It can be clearly understood from Eq. (24) that disturbances will amplify when the growth rate is real and positive thereby requiring $kR < 1$ and the maximum growth rate ω_{max} occurs for $kR = 0.697$. Substituting all the known parameters in Eq. (24), ω_{max} comes out to be 73.016 s^{-1}. Having obtained ω_{max}, a relationship can

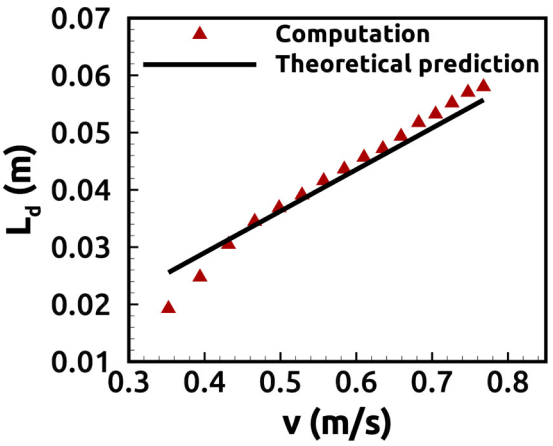

FIG. 10. Variation of computed jet breakup length along with predictions from theory [Eq. (25)] as a function of inflow velocity. The breakup length show very good agreement with the analytical results of Rayleigh's theory.

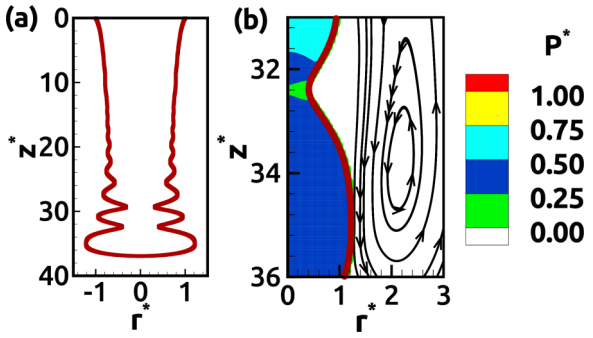

FIG. 11. (a) Instantaneous jet radius as a function of downstream distance showing varicose undulations on its surface. The radial direction has been magnified for clear visualization of the perturbations. (b) Closeup view of the jet between $z^* = 31$ and $z^* = 36$ showing pressure contours and also streamlines in the ambient air. A vortex is seen developing just outside the jet indicating air entrainment. The relevant parameters are We = 3.0, Oh = 0.003, and Bo = 0.18.

be determined to predict the breakup length as a function of inflow velocity as [41]

$$L = v_{\text{avg}}\, t$$
$$t = C/\omega_{\max}$$
$$L = C\, v_{\text{avg}}/\omega_{\max}, \tag{25}$$

where L is the breakup length of the jet, t is the breakup time and C is a constant defined as $C = \ln(R/a)$, a being the amplitude of perturbation applied to the interface.

In our present study, Bo and Oh are fixed at 0.18 and 0.003 while We is progressively increased by varying the inflow velocity. The breakup of the jets occurs experimentally as a result of naturally occurring perturbations. Homma *et al.* [72] reported that a source of disturbance is generated during the early stages of jet formation when the interface evolves from the initially assumed shape to a liquid column in the numerical simulations. Thus, the hypothesis of Rayleigh that growth of infinitesimal disturbances leads to breakup is satisfied without any externally imposed perturbations. However, the precise magnitude of this disturbance is not known. As such, a temporal sinusoidal perturbation of amplitude a and angular frequency ω was introduced in the inflow velocity. The angular frequency is obtained from Eq. (24) corresponding to maximum growth rate and the amplitude a is taken as $0.005R$. The limiting length of jet at breakup L_d computed from our simulations is plotted along with the theoretical predictions from Eq. (25) as a function of average inlet velocity v_{avg} and shown in Fig. 10. The value of constant C is found to be 5.98 from the present computations. The theoretical value of C corresponding to an externally applied perturbation of amplitude $a = 0.005R$ is 5.2, which is close to the numerically obtained value of 5.98. The constant C has an inverse relationship with the amplitude of applied disturbance. As the perturbation amplitude increases, the value of C decreases and hence the breakup length decreases. García *et al.* [73,74] also reported that the breakup length decreases with increase in the amplitude of the disturbance, which agrees well with our current observations. It can be obviously discerned that the values of L_d obtained from present computations agree well with the predictions owing to Rayleigh's theory given by Eq. (25) for $v_{\text{avg}} > 0.53\ m/s$, which corresponds to We > 4.5. It is to be noted from Eq. (16) that We for our study is defined based on the orifice radius whereas in Eq. (23), We has been defined based on the orifice diameter. Hence, the effective value of We_l above which good agreement with Rayleigh's theory is observed in our computations occurs at $\text{We}_l > 9$. The result matches closely with the criterion given in Eq. (23). Due to the very small density of air, We_g remains less than 0.4 for the entire range of our study.

A snapshot is taken from the simulation of jet breakup at an arbitrary time instant under the conditions of Oh = 0.003, Bo = 0.18, and We = 3.0 as illustrated in Fig. 11 (a). No external perturbation is applied in this case. Similar observations were reported by Pan and Suga [19] during simulation of jet breakup in the Rayleigh regime without having applied any external perturbations. The radial coordinate has been magnified to clearly display the surface oscillations present on the liquid jet. These varicose-shaped undulations emerge from upward wave propagation on the jet surface after drops pinch off from it. It may be noted that Taylor [75] also studied waves on a fluid sheet where surface tension effects are dominant compared to gravity and aerodynamic effects. He showed that these capillary waves are of two types—symmetrical waves in which displacement of opposite surfaces are in opposite directions and antisymmetrical waves in which displacements at corresponding points of opposite surfaces are in same direction [32]. As the inertia effects become more and more dominant with increasing We, the interaction with the ambient medium can no longer be neglected. A jet injected into quiescent air has a liquid-air interface on the surface of the column, which can result in perturbations to a quasistable flow situation owing to aerodynamic drag, friction, and flow turbulence. Figure 11(b) presents a closeup view of the jet showing the contours of nondimensional pressure P^* and also the streamlines in the ambient medium. It can be easily observed that a sharp jump of pressure exists between the outer medium and the inside of the jet. Also, a gradient of pressure exists as we move downstream towards the neck

region, which facilitates drop breakup. Additionally, a closer look at the streamline plot in the ambient air reveals a vortical structure on the side of the jet. This growing vortex signifies that the ambient air is entrained as the jet elongates downstream and this air entrainment increases with increasing We. The growing interaction of the ambient air with the liquid jet will finally cause transition from the Rayleigh regime to first wind-induced regime where sinuous waves start appearing on the jet surface thereby deviating from axisymmetric flow behavior. Hence, we limit our computations to the Rayleigh regime and the flows with higher throughput fall beyond our scope of study.

V. SUMMARY

Numerical simulations of formation of drops and breakup of liquid jets from an orifice are performed using CLSVOF method under axisymmetric conditions. In the context of understanding free-surface flows, the study provides physical insight into the dynamics of drop formation from orifices. The analysis forms the basis for many intricate technologies, such as inkjet printing, spraying, and atomization.

The study focuses on the growth history of a drop under constant inflow conditions and presents a quantitative match with a theoretically predicted growth law. The profile of the drop during the initial growth stage is showed to be self-similar, which serves as an addition to the existing knowledge on self similarity near the collapse stage, reported earlier in the literature. The thinning behavior of the liquid neck shows a transition from an inertia-dominated regime to an inertia-viscous regime when the liquid neck falls below a critical minimum radius. It is observed that interface overturning occurs when drop viscosity is low whereas it is arrested for highly viscous drops. A detailed parametric study of the overturning phenomenon reveals a critical value of $\mathrm{Oh} = 0.075$ above which overturning stops. The numerically predicted values of large and small cone angles of the interface matches well with the theoretically predicted values for small Oh. However, the numerical predictions deviate significantly from the theoretically predicted values of 112.8° and 18.1° as the drop viscosity is increased. The transition from dripping to jetting regime has been simulated and two distinct jetting regimes have been observed depending on the dominance of inertia or viscous forces. The increased injection rate of drop liquid causes a transition to jetting regime, which can be explained in terms of the dominance of inertia force over capillary force. Another class of transition occurs due to the increased viscosity of the exterior fluid, which increases the viscous drag on the interior liquid stream entailing transition to jetting. The radii of the drops formed in this regime are significantly larger than the jet radius. The jetting profile under the dominance of viscous effects shows a profoundly different behavior compared to the results reported earlier and thus serves as an addition to the existing insight on the transition from dripping to jetting. The jet length at breakup, computed from our simulations, corroborates the predictions from Rayleigh's theory in the jetting regime. Varicose perturbations are observed on the surface of the liquid column as the jet moves downstream. The high inertia of the moving jet causes entrainment of ambient air resulting in a vortical structure just outside the liquid jet. The entrainment increases as the We is increased signifying the influence of the ambience on the dynamics of breakup at higher inflow rates. The observations from the present analysis may stimulate further investigations on such systems through more comprehensive three-dimensional simulations in the near future.

[1] T. W. Shield, D. B. Bogy, and F. E. Talke, IBM J. Res. Dev. **31**, 96 (1987).
[2] J. Eggers and E. Villermaux, Rep. Prog. Phys. **71**, 036601 (2008).
[3] W. J. Heideger and M. W. Wright, AIChE J. **32**, 1372 (1986).
[4] O. A. Basaran, AIChE J. **48**, 1842 (2002).
[5] S. D. R. Wilson, J. Fluid Mech. **190**, 561 (1988).
[6] X. Zhang and O. A. Basaran, Phys. Fluids **7**, 1184 (1995).
[7] D. M. Henderson, W. G. Pritchard, and L. B. Smolka, Phys. Fluids **9**, 3188 (1997).
[8] C. Clanet and J. C. Lasheras, J. Fluid Mech. **383**, 307 (1999).
[9] H. J. Subramani, H. K. Yeoh, R. Suryo, Q. Xu, B. Ambravaneswaran, and O. A. Basaran, Phys. Fluids **18**, 32106 (2006).
[10] B. Ambravaneswaran, E. D. Wilkes, and O. A. Basaran, Phys. Fluids **14**, 2606 (2002).
[11] B. Ambravaneswaran, H. J. Subramani, S. D. Phillips, and O. A. Basaran, Phys. Rev. Lett. **93**, 034501 (2004).
[12] B. Ambravaneswaran, S. D. Phillips, and O. A. Basaran, Phys. Rev. Lett. **85**, 5332 (2000).
[13] J. Eggers and T. F. Dupont, J. Fluid Mech. **262**, 205 (1994).
[14] R. Schulkes, J. Fluid Mech. **278**, 83 (1994).
[15] D. F. Zhang and H. A. Stone, Phys. Fluids **9**, 2234 (1997).
[16] O. E. Yildirim, Q. Xu, and O. A. Basaran, Phys. Fluids **17**, 062107 (2005).
[17] A. U. Chen, P. K. Notz, and O. A. Basaran, Phys. Rev. Lett. **88**, 174501 (2002).
[18] Z. Che, T. N. Wong, N.-T. Nguyen, Y. F. Yap, and J. C. Chai, Chem. Eng. Sci. **66**, 5293 (2011).
[19] Y. Pan and K. Suga, Phys. Fluids **18**, 052101 (2006).
[20] W. D. Harkins and F. E. Brown, J. Am. Chem. Soc. **41**, 499 (1919).
[21] J. R. Castrejón-Pita, A. A. Castrejón-Pita, S. S. Thete, K. Sambath, I. M. Hutchings, J. Hinch, J. R. Lister, and O. A. Basaran, Proc. Natl. Acad. Sci. **112**, 4582 (2015).
[22] A. M. Lakdawala, R. Thaokar, and A. Sharma, Sadhana **40**, 819 (2015).
[23] F. Savart, Ann. Chim. Phys. **53**, 337 (1833).
[24] L. Rayleigh, P. Lond. Math. Soc. **s1**, 4 (1878).
[25] L. Rayleigh, Lond. Edi. Dub. Phil. Mag. J. Sci. **34**, 145 (1892).
[26] C. Weber, Z. angew. Math. Mech. **11**, 136 (1931).
[27] S. Tomotika, Proc. R. Soc. London A **150**, 322 (1935).
[28] G. I. Taylor, *The Scientific Papers of G. I. Taylor*, Vol. 3 (Cambridge University Press, Cambridge, 1940).
[29] H. B. Squire, Br. J. Appl. Phys. **4**, 167 (1953).

[30] S. Chandrasekhar, *Hydrodynamic and Hydromagnetic Stability* (Dover, New York, 1961).
[31] A. M. Sterling and C. A. Sleicher, J. Fluid Mech. **68**, 477 (1975).
[32] G. Biswas, S. K. Som, and A. S. Gupta, J. Fluids Eng. **107**, 451 (1985).
[33] Y. D. Shikhmurzaev, IMA J. Appl. Math. **70**, 880 (2005).
[34] B. J. Meister and G. F. Scheele, AIChE J. **15**, 689 (1969).
[35] B. J. Meister and G. F. Scheele, AIChE J. **15**, 700 (1969).
[36] A. H. P. Skelland and K. R. Johnson, Can. J. Chem. Eng. **52**, 732 (1974).
[37] R. J. Donnelly and W. Glaberson, in *Proceedings of the Royal Society of London A: Mathematical, Physical and Engineering Sciences*, Vol. 290 (The Royal Society, London, 1966), pp. 547–556.
[38] R. P. Grant and S. Middleman, AIChE J. **12**, 669 (1966).
[39] R. W. Fenn and S. Middleman, AIChE J. **15**, 379 (1969).
[40] E. F. Goedde and M. C. Yuen, J. Fluid Mech. **40**, 495 (1970).
[41] I. L. Omocea, C. Patrascu, M. Turcanu, and C. Balan, Energy Procedia **85**, 383 (2016).
[42] J. R. Richards, A. M. Lenhoff, and A. N. Beris, Phys. Fluids **6**, 2640 (1994).
[43] J. R. Richards, A. N. Beris, and A. M. Lenhoff, Phys. Fluids A **5**, 1703 (1993).
[44] J. L. Duda and J. S. Vrentas, Chem. Eng. Sci. **22**, 855 (1967).
[45] Y. Pan and K. Suga, J. Fluids Eng. **125**, 922 (2003).
[46] J. Delteil, S. Vincent, A. Erriguible, and P. Subra-Paternault, Comput. Fluids **50**, 10 (2011).
[47] I. Chakraborty, G. Biswas, and P. S. Ghoshdastidar, Int. J. Heat Mass Transf. **58**, 240 (2013).
[48] I. Chakraborty, B. Ray, G. Biswas, F. Durst, A. Sharma, and P. S. Ghoshdastidar, Phys. Fluids **21**, 062103 (2009).
[49] I. Chakraborty, G. Biswas, and P. S. Ghoshdastidar, Int. J. Heat Mass Transf. **54**, 4673 (2011).
[50] B. Ray, G. Biswas, and A. Sharma, J. Fluid Mech. **655**, 72 (2010).
[51] B. Ray, G. Biswas, and A. Sharma, Phys. Fluids **24**, 082108 (2012).
[52] B. Ray, G. Biswas, and A. Sharma, J. Fluid Mech. **768**, 492 (2015).
[53] G. Tomar, G. Biswas, A. Sharma, and S. Welch, Phys. Fluids **20**, 092101 (2008).
[54] J. U. Brackbill, D. B. Kothe, and C. Zemach, J. Comput. Phys. **100**, 335 (1992).
[55] M. Sussman and E. G. Puckett, J. Comput. Phys. **162**, 301 (2000).
[56] S. Osher and J. A. Sethian, J. Comput. Phys. **79**, 12 (1988).
[57] C. W. Hirt and B. D. Nichols, J. Comput. Phys. **39**, 201 (1981).
[58] F. H. Harlow and J. E. Welch, Phys. Fluids **8**, 2182 (1965).
[59] Y.-C. Chang, T. Y. Hou, B. Merriman, and S. Osher, J. Comput. Phys. **124**, 449 (1996).
[60] D. Gerlach, G. Tomar, G. Biswas, and F. Durst, Int. J. Heat Mass Transf. **49**, 740 (2006).
[61] B. Nath, G. Biswas, A. Dalal, and K. C. Sahu, Phys. Rev. E **95**, 033110 (2017).
[62] V. Pandey, G. Biswas, and A. Dalal, Phys. Fluids **29**, 032104 (2017).
[63] A. Rothert, R. Richter, and I. Rehberg, Phys. Rev. Lett. **87**, 084501 (2001).
[64] E. D. Wilkes, S. D. Phillips, and O. A. Basaran, Phys. Fluids **11**, 3577 (1999).
[65] R. F. Day, E. J. Hinch, and J. R. Lister, Phys. Rev. Lett. **80**, 704 (1998).
[66] J. R. Castrejón-Pita, A. A. Castrejón-Pita, E. J. Hinch, J. R. Lister, and I. M. Hutchings, Phys. Rev. E **86**, 015301(R) (2012).
[67] A. S. Utada, A. Fernandez-Nieves, H. A. Stone, and D. A. Weitz, Phys. Rev. Lett. **99**, 094502 (2007).
[68] S. P. Lin and R. D. Reitz, Annu. Rev. Fluid Mech. **30**, 85 (1998).
[69] N. Chigier and R. D. Reitz, in *Recent Advances in Spray Combustion: Spray Atomization and Drop Burning Phenomena*, edited by K. Kuo (AIAA, Reston, 1996).
[70] J. Plateau, *Experimental and Theoretical Statics of Liquids Subject to Molecular Forces Only* (Gauthier-Villars, Paris, 1873).
[71] J. W. M. Bush, MIT Lecture Notes on Surface Tension, Lecture 5, Massachusetts Institute of Technology, 2004 (unpublished).
[72] S. Homma, J. Koga, S. Matsumoto, and G. Tryggvason, Theor. Appl. Mech. Jpn. **51**, 241 (2002).
[73] F. García, H. González, J. Castrejón-Pita, and A. Castrejón-Pita, Appl. Phys. Lett. **105**, 094104 (2014).
[74] F. J. García and H. González, J. Fluid Mech. **602**, 81 (2008).
[75] G. Taylor, Proc. R. Soc. Lond. A **253**, 296 (1959).